Model-based control design for H_2 purity regulation in high-pressure alkaline electrolyzers

Martín David[a,b,*], Fernando Bianchi[a], Carlos Ocampo-Martinez[b], Ricardo Sánchez-Peña[a]

[a] *Instituto Tecnológico Buenos Aires (ITBA) and Consejo Nacional de Investigaciones Científicas y Técnicas (CONICET), Ciudad Autónoma de Buenos Aires, Argentina*
[b] *Automatic Control Department, Universitat Politècnica de Catalunya, Institut de Robòtica i Informàtica Industrial (CSIC-UPC), Barcelona, España*

Abstract

This paper proposes two control strategies that mitigate the cross contamination of H_2 and O_2 in a high-pressure alkaline electrolyzer, which consequently increases the supplied gases purity: one based on a decoupled PI scheme and the other based on optimal control tools. In order to reduce the diffusion of gases through the membrane, the controllers establish the opening of two outlet valves based on the pressure of the system and the difference in liquid level between both separation chambers. Therefore, two multiple input - multiple output controllers are designed here. For this purpose, a high-fidelity model previously developed was simplified in order to obtain a control-oriented model. The proposed controllers were evaluated in simulation using the high-fidelity nonlinear model in a wide operating range, which resulted in less than 1% impurity of gases.

Keywords: Hydrogen, alkaline electrolysis, multivariable control, $\mathcal{H}_\infty$ optimal control

1. Introduction

The world economy is constantly expanding along with the demand for energy [1]. Furthermore, the extensive use of fossil fuels, with the consequent

*Corresponding author
Email address: mdavid@itba.edu.ar (Martín David)

emission of greenhouse gases, is widely accepted as a situation that needs to change. In this line, global impact studies and environmental protection policies have been formulated [2, 3]. Around the world, solutions focused on renewable energy sources have been proposed in order to mitigate the emission of greenhouse gases due to the intensive use of fossil fuels. However, the ability to accumulate the excess of energy over long periods of time is needed in order to reach a high integration of renewable energy sources. A widely accepted idea is the use of hydrogen as an energy vector, known as the *hydrogen economy*, which would be an integral solution to produce, store and supply energy [4, 5, 6].

Among all the methods of producing sustainable hydrogen, the alkaline electrolysis is presented as the most available technology. Currently, there is a renewed interest in this technology due to its ease of connection to renewable energy sources [7]. Commonly, the combination of electrolyzers, storage tanks and fuel cells is used as an energy buffer [8, 9]. Alkaline electrolysis consists in the separation of water to form H_2 and O_2 by applying an electric current. The electrolytic cell consists of a pair of electrodes and a membrane made of Zirfon^{TM} that prevent gas mixing. One of the most important challenges of the alkaline electrolysis is the diffusion through this membrane driven by differences in concentration and pressure [10]. Although the first cause of cross-contamination is inherent in the process and is related to the development of new membranes, the pressure differential can be mitigated by a suitable control design actuating over the outlet valves of both separating chambers.

Despite alkaline electrolysis is a mature technology, its mathematical modelling is still under development. Most models focus only on the cell-stack description but not in the entire system [11, 12, 13]. Moreover, most of them describe the stationary regime and are built from empirical equations [14, 15, 16]. Recently, Sanchez et al [17] used a commercial software to model the entire system while the cell-stack is described by a semi-empirical approach. In the same direction, some of the authors of the current work have developed a Phenomenological Based Semi-empirical Model (PBSM) reported in [18, 19]. This model has the advantage of describing the dynamic phenomena and the evolution of all the electrolyser subsystems.

Furthermore, to the best of the authors' knowledge, and also from the conclusions reported by Olivier et al [20], the design of controllers to solve the problem mentioned above seems to be not addressed yet in the literature. Therefore, the development of useful input-output models for control design

is an open research topic [20]. In general, control objectives are completely focused on the management of the electrolyzer as an electrical consumer and producer of H_2 connected to a grid [21, 22]. Moreover, the control of the outlet valves could be found mentioned only by Schug in his description of a pilot plant [23]. In his work, an alkaline electrolyzer is described in detail along with experimental results. However, the control system is not detailed enough, but the connection of plant output with control action can be recognized in the simplified flow diagram presented.

Given the lack of control strategies designed for such systems and, in particular, those strategies based on suitable and reliable (dynamic) models properly obtained for control tasks, the main contribution of this paper is twofold. First, from a well-established nonlinear model considering the dynamics and the accurate phenomenology of the alkaline electrolyzers reported in [19], a reduced model able to be used as a control-oriented model (COM) is obtained and properly validated by using the complete nonlinear model (which, in turn, is validated with real data). Second, by using the reduced model, two controllers are designed and the closed-loop performance of the system is compared based on the maximization of the hydrogen purity through the mitigation of the cross-contamination of gases into the chambers.

The remainder of the work is structured as follows. A description of a high-pressure alkaline electrolyzer is presented in Section 2. Next, in Section 3, two controllers are designed, a multivariable PI controller and an optimal model-based one. Simulation results comparing both controllers are presented and discussed in Section 4. At the end, some final comments are gathered in Section 5.

2. High-pressure alkaline electrolyzer

As previously mentioned, a proposed solution for energy storage is the combination of an electrolyzer, storage tanks and a fuel cell. In this way, the additional electrical energy is used to produce hydrogen that is stored in the tanks. When renewable energy sources are not able to meet the demand, the stored hydrogen is consumed by the fuel cell.

High-pressure alkaline electrolyzers can supply gases at a storage pressure, dispensing with the use of compressors. However, cross-contamination, i.e., the concentration of O_2 in the H_2 stream and vice versa, increases with pressure, then special attention is required in operation due to safety and quality issues.

Figure 1 shows the piping and instrumentation of a high-pressure alkaline electrolyzer prototype. The components of this system are:

- a pressurized tank (PT) that contains a pack of 15 alkaline electrolytic cells;
- two independent KOH solution circuits with recirculation pumps;
- two gas separation chambers (SC) where the produced gas is split from the liquid KOH solution;
- two heat exchangers for both circuits (HEO and HEH);
- a water injection pump that periodically replenishes the consumed water;
- two outlet lines controlled by two motorized valves (MVO and MVH) connected to storage tanks; and
- an equalization line that connects both bottoms of the SCs.

A detailed description of this system is presented in [18, 19].

As mentioned in the Introduction, the main objective of an alkaline electrolyzer is to separate water to form H_2 and O_2 by applying an electric current I. In this process, it is highly important to minimize the diffusion through the membrane caused by differences in both concentration and pressure. Up to 2% of H_2 in the O_2 stream is widely accepted as a limit, taking into account that the lower explosive limit of H_2 is 4%. Additionally, H_2 and O_2 gases must be delivered at high pressures in order to avoid the use of compressors. Since gas purity decreases with higher pressures, it is expected to increase the possible operating pressure preventing contamination with a suitable control strategy.

2.1. Cross-contamination

As stated before, the main difficulty in the operation of an alkaline electrolyzer is the contamination of both streams, especially on the O_2 side. Generally, this concept is approached in the models as an empirical equation that relates contamination to the state of the system (e.g., current density, temperature, pressure). This way evidences the lack of dynamic analysis of purity. However, there are studies that analyze the phenomenology of the

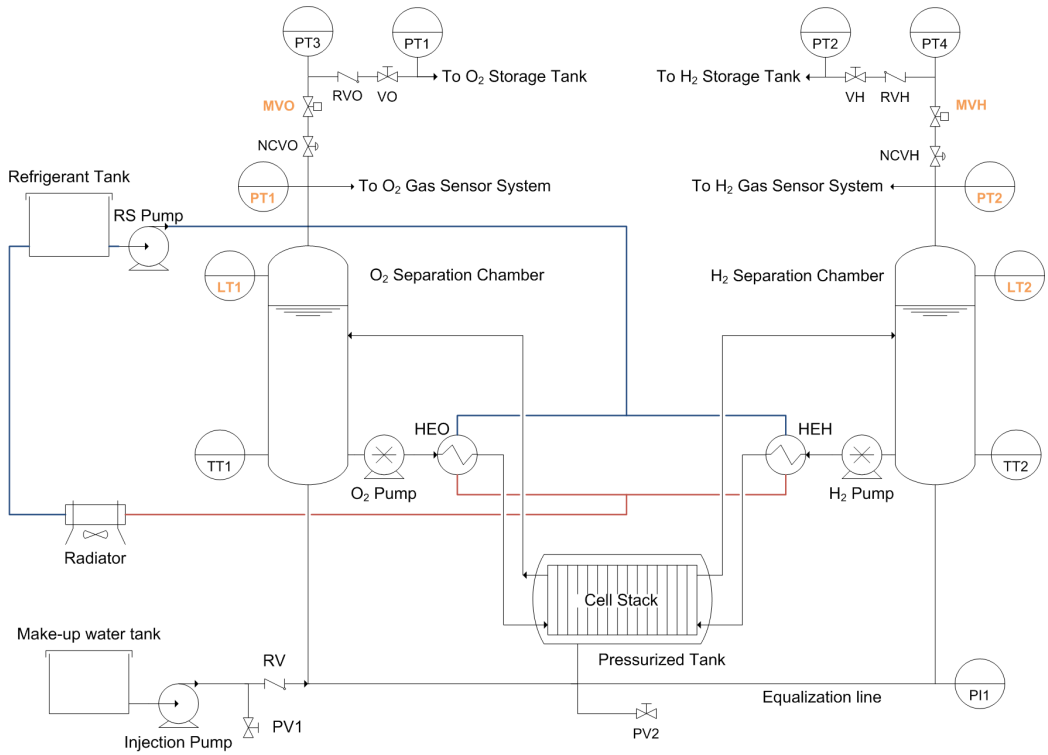

Figure 1: Piping and instrumentation diagram of the high-pressure alkaline electrolyzer. The main sensors and actuators explained in the text are highlighted in orange. Adapted from [19]

contamination process as [10] which is used into the phenomenological based semi-physical model reported in [19].

Electrolysis process happens in the electrolytic cell that is represented in Figure 2. Each cell is formed by two electrodes and a membrane which separates both half cells. There are two driving forces for gas cross-permeation through this membrane. The first one is diffusion driven by differences in dissolved gas concentration between the two half cells [24]. This phenomenon can be modelled on the basis of Fick's law as

$$\Phi_{c\rightarrow a,Fick} = D_{\mathrm{H_2}} \frac{C_{\mathrm{H_2},c} - C_{\mathrm{H_2},a}}{z_{cell}}, \tag{1}$$

being $\Phi_{c\rightarrow a,Fick}$ the $\mathrm{H_2}$ flux from cathode (c) to anode (a), $D_{\mathrm{H_2}}$ the diffusion coefficient of $\mathrm{H_2}$ through the separator, $C_{\mathrm{H_2},x}$ the $\mathrm{H_2}$ concentration in both half cells and z_{cell} the separator width. The presented equation corresponds

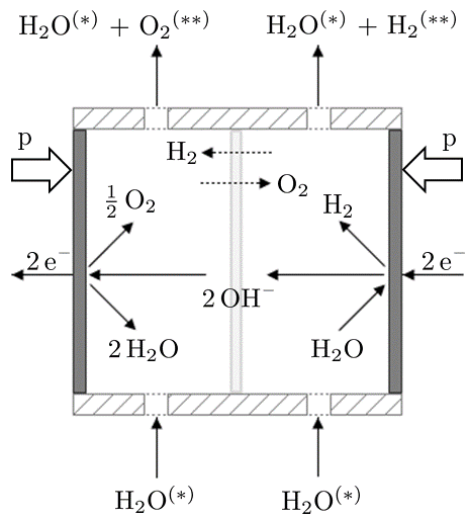

Figure 2: Scheme of the electrolytic cell with reactions. $H_2O^{(*)}$ represents KOH solution and $O_2^{(**)}$ and $H_2^{(**)}$ represent outputs that are contaminated with H_2 and O_2, respectively. Taken from [19]

to the H_2 diffusion, a similar equation can be described for the O_2.

The second cause of cross-contamination is the permeability of the electrolyte with dissolved gases due to differential pressure between both half cells. Based on Darcy's law, H_2 flux when cathodic pressure is higher than anodic one can be written as

$$\Phi_{c\to a,Darcy} = \epsilon_{H2}^{Darcy} \frac{P_c - P_a}{z_{cell}}, \tag{2}$$

where $\Phi_{c\to a,Darcy}$ is the H_2 flux from cathode to anode when cathodic pressure P_c is greater than anodic pressure P_a. The H_2 permeability ϵ_{H2}^{Darcy} depends on fluid properties and the concentration of dissolved H_2. In case anodic pressure is greater than the cathodic one, a similar equation can be obtained for the O_2 contamination flux. Clearly, only one flux occurs at a time.

2.2. Control scheme

An alkaline electrolyzer requires several control loops for an efficient and safe operation. The control of both the refrigeration system and the make-up pump ensures a safe operation of the electrolyzer. Whereas, the H_2 production is controlled by the outlet valves. This paper is focused on the latter. A brief description of the other loops is described next.

The refrigeration system and the make-up pump are controlled independently by hysteresis cycles. These control loops, whose designs are not going to be treated in this paper, are defined by the following sets of constraints:

$$\begin{aligned} L_{\mathrm{H_2}} \leq L_{\min} \text{ and } L_{\mathrm{O_2}} \leq L_{\min} \Rightarrow u_{\mathrm{pump}} = 1, \\ L_{\mathrm{H_2}} \geq L_{\max} \text{ or } L_{\mathrm{O_2}} \geq L_{\max} \Rightarrow u_{\mathrm{pump}} = 0, \end{aligned} \tag{3}$$

$$\begin{aligned} T_{\mathrm{H_2}} + T_{\mathrm{O_2}} \geq 2\, T_{\max} \Rightarrow u_{RS} = 1, \\ T_{\mathrm{H_2}} + T_{\mathrm{O_2}} \leq 2\, T_{\min} \Rightarrow u_{RS} = 0, \end{aligned} \tag{4}$$

where $L_{\mathrm{O_2}}$, $L_{\mathrm{H_2}}$, $T_{\mathrm{O_2}}$ and $T_{\mathrm{H_2}}$ are the liquid solution levels and temperatures in O_2 and H_2 SCs, respectively. These variables are measured by the transmitters LT1, LT2, TT1 and TT2, respectively (see Figure 1). The limits imposed are $L_{\min} = 0.45$ m, $L_{\max} = 0.5$ m, $T_{\min} = 39.5$ °C and $T_{\max} = 40.5$ °C. Finally, the control actions u_{pump} and u_{RS} manage the activation of the injection pump, the refrigeration system pump and the radiator, respectively.

Finally, energy management, with the consequent control of the current-voltage relationship, is intrinsically related to the power sources, so it is beyond the scope of this paper. Details on this topic can be found in [12, 17, 25].

As previously indicated, in alkaline electrolysis, a pressure difference between both half-cells generates the gas crossover. Therefore, the control objective is to keep the liquid solution levels equalized in both SCs (measured by LT1 and LT2 in Figure 1) while H_2 and O_2 are delivered at a certain pressure (measured by PT1 and PT2 in Figure 1). This objective is achieved acting over two motorized outlet valves (MVO and MVH in Figure 1). The operating ranges for pressure p and electric current I are 0-7000 kPa and 10-50 A, respectively. It is important to note that this electrolyzer, with an electrode area of $A_{cell} = 143$ cm^2, works in a current density j range between 70-350 mA/cm^2 under the direct relationship

$$j = \frac{I}{A_{cell}}. \tag{5}$$

With the aim of having a suitable resolution in these wide operating ranges and considering the H_2 production capacity of 0.5 Nm^3/h, needle-type outlet valves with a relatively small maximum flow coefficient, e.g., $C_v = 0.004$, must be used. In order to be able to control the system with only one valve per outlet line, the pressure in both storage tanks should be similar.

Another variable to be controlled is the difference between the liquid levels in both SCs, defined as

$$\Delta L = L_{\mathrm{H_2}} - L_{\mathrm{O_2}}. \tag{6}$$

This variable must be kept around a set-point $\Delta L_{\mathrm{ref}} = 0$. This condition will contribute to the natural action of the equalization line circuit by keeping the pressure equalized on both sides of the membrane. In other words, if the control dynamics are slow enough, the equalization line ensures that the pressure in both SCs is almost the same, and the same happens in the electrolytic cells. As stated by Schalenbach et al [10], the Zirfon^{TM} membrane is highly permeable to pressure differences, which was described in Section 2.1. These pressures P_c and P_a depend on the pressure of each SC and the pressure exerted by the column of liquid. In order to understand the effect of the liquid level difference in each SC, an example is presented next. A difference in level $\Delta L = 2$ mm represents a pressure difference of 25 Pa. Considering only this difference, a contaminating flow of H_2 from cathode to anode $\dot{n}_5 = 1.71 \times 10^{-9}$ kmol s^{-1} occurs (see Figure A.11). The purity of the gases produced will depend on the rate of O_2 production. Therefore, with a low current density $j = 70$ mA/cm^2, an impurity of 0.24 % will be obtained. Finally, controlling the difference in level and pressure generates a high purity of the supplied gases. However, the absence of contamination is unreachable due to the natural diffusion that occurs in the studied process.

The control scheme proposed to achieve the objectives is presented in Figure 3. The controller produces two valve opening values, $u_{\mathrm{H_2}}$ and $u_{\mathrm{O_2}}$, taking values between 0 (minimum opening) and 10 (maximum opening). The control values are computed to ensure that

$$P_{\mathrm{H_2}} \to P_{\mathrm{ref}}, \tag{7a}$$

$$\Delta L \to 0. \tag{7b}$$

In normal operation, this pressure is set externally in order to follow smoothly the pressure of the storage tanks P_{tank}. Accordingly, the reference for the pressure P_{ref} is defined as

$$P_{\mathrm{ref}} = P_{\mathrm{tank}} + P_{gap}, \text{ subject to } |dP_{\mathrm{ref}}/dt| < \alpha, \tag{8}$$

being α a rate limit in kPa/s. This rate limit ensures that a sudden change in the storage pressure does not generate an excessive variation in the pressure at both sides of the membrane, with the consequent cross-contamination.

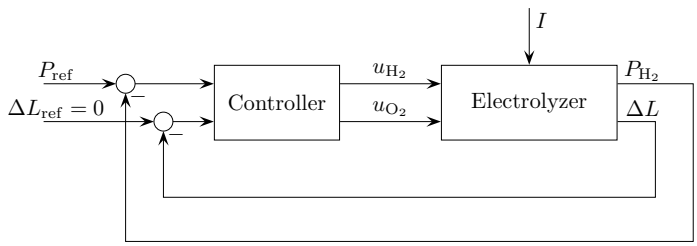

Figure 3: Proposed control scheme.

Under the assumption of similar pressures, P_{tank} is set equal to P_{H_2}. Moreover, the pressure gap between P_{ref} and P_{tank}, $P_{\text{gap}} = 50$ kPa, is needed to compensate the action of the retention valves (RVO and RVH).

The described control loops act simultaneously and independently. For instance, when the make-up pump acts injecting water, the main loop developed in this work equalizes the levels by either opening or closing the valves. Then, the action of the former (make-up pump) appears as a disturbance to the latter (outlet valves).

2.3. Reduced control-oriented model

A highly-detailed model for alkaline electrolyzers is given in [18, 19]. This model has 25 differential equations (i.e., 25 states) and 17 additional variables, 50 structural parameters and 49 functional parameters. The basic structure of Ordinary Differential Equations (ODEs) is presented in the Appendix and a complete description can be found in the aforementioned references.

Such a model is suitable for simulation purposes but not for control design. To this end, those variables that produce smaller effects on the controlled variables (ΔL and P_{H_2}) might be neglected under some assumptions and guaranteed conditions that are explained next.

- Although the ultimate goal is to maximize the purity of the gases, the concentrations of impurities are not taken into account for the controller, which is based on the liquid levels and the system pressure.

- In addition, despite having two paths of diffusion, i.e., through the membrane and through the equalization line, the latter is smaller than the former (10^6 times). This is mainly due to a longer path through the

equalization line (approximately 3 m) against just the thickness of the membrane (approximately 5×10^{-4} m). Then, the diffusion through the equalization line can be neglected along with the corresponding states.

- Moreover, under the hypothesis of reaching gas purities greater than 99%, saturation of pure gas in each cell can be assumed in order to calculate diffusion across the membrane.

- Furthermore, according to the ideal gas law, the gas moles behave equally no matter the substance, hence it only matters the accountancy of the number of moles at each line.

- Finally, only the concentrations of pure gases in the electrolytic cells and in the SCs can be considered.

Based on the previous assumptions, the model can be reduced to 14 states. The ODEs corresponding to these 14 states are listed in Table 1. The rest of the states are considered constant while the parameters, which are represented by algebraic equations, are not modified.

Different scenarios with pulse-type signals in the disturbances i and P_{tank} and control inputs u_{H_2} and u_{O_2} were simulated to compare the responses of the original model and the reduced COM. Figure 4 shows the results of one of them when the initial operating conditions correspond to $I = 30$ A and $P_{\text{H}_2} = 4000$ kPa (an operating point in the center of the considered operating range) and only a pulse-type signal in the current is applied. The duration of that pulse was 10 s and the amplitude was 30 A. In the top-plot of Figure 4, the evolutions of the pressure P_{H_2} for the full original model (solid black line) and the same pressure for the reduced COM (dashed red line) can be observed. The second and third plots compare the evolutions of the levels L_{H_2} and L_{O_2}, respectively. The bottom plot shows the difference of levels ΔL for the original and the reduced models, respectively. The relative errors[1] for the pressure and each level, and the absolute error, in case of the level difference, can be seen in solid blue lines. In this last case, the nominal values are close to zero and the relative error is impractical. Notice that the maximum approximation error is 2×10^{-5} m in ΔL, which is quite small comparing with the maximum value of this signal in Figure 4. In all cases,

[1]The relative error is defined as $100\,|y_{\text{original}} - y_{\text{reduced}}|/|y_{\text{original}}|$

Table 1: ODEs corresponding to the reduced nonlinear model.

State	Corresponding ODE
1	$\frac{d\bar{\rho}_3}{dt} = \frac{1}{V_{mix,I}} \left(\dot{n}_1 + \dot{n}_{22} + \dot{n}_6 - \dot{n}_3 - \dot{n}_5 - \dot{n}_{21} + r \sum_i \sigma_{i,1}\right)$
2	$\frac{dx_{\mathrm{H_2},3}}{dt} = \frac{1}{N_I} \left(x_{\mathrm{H_2},1}\, \dot{n}_1 - x_{\mathrm{H_2},3}\, \dot{n}_3 - \dot{n}_5 + \dot{n}_6 + r_1 - x_{\mathrm{H_2},3}\, \dot{N}_I\right)$
3	$\frac{d\bar{\rho}_4}{dt} = \frac{1}{V_{mix,II}} \left(\dot{n}_2 - \dot{n}_{22} - \dot{n}_6 - \dot{n}_4 + \dot{n}_5 + \dot{n}_{21} + r \sum_i \sigma_{i,2}\right)$
4	$\frac{dx_{\mathrm{O_2},4}}{dt} = \frac{1}{N_{II}} \left(x_{\mathrm{O_2},2}\, \dot{n}_2 + \dot{n}_5 - \dot{n}_6 - x_{\mathrm{O_2},4}\, \dot{n}_4 + \frac{r}{2} - x_{\mathrm{O_2},4}\, \dot{N}_{II}\right)$
5	$\frac{dN_{III}}{dt} = \dot{n}_3 + \dot{n}_7 - \dot{n}_9 - \dot{n}_{11}$
6	$\frac{dL_{Lg,III}}{dt} = \frac{1}{A_{SC}} \left(\dot{V}_3 + \dot{V}_7 - \dot{V}_9 - \dot{V}_{11} + \dot{V}_{b,III}\right)$
7	$\frac{dx_{\mathrm{H_2},III}}{dt} = \frac{1}{N_{III}} \left(x_{\mathrm{H_2},3}\, \dot{n}_3 + x_{\mathrm{H_2},7}\, \dot{n}_7 - \dot{n}_9 - x_{\mathrm{H_2},11}\, \dot{n}_{11} - x_{\mathrm{H_2},III}\, \dot{N}_{III}\right)$
8	$\frac{dN_{IV}}{dt} = \dot{n}_4 - \dot{n}_8 - \dot{n}_{10} - \dot{n}_{12}$
9	$\frac{dL_{Lg,IV}}{dt} = \frac{1}{A_{SC}} \left(\dot{V}_4 - \dot{V}_8 - \dot{V}_{10} - \dot{V}_{12} + \dot{V}_{b,IV}\right)$
10	$\frac{dx_{\mathrm{O_2},IV}}{dt} = \frac{1}{N_{IV}} \left(x_{\mathrm{O_2},4}\, \dot{n}_4 - x_{\mathrm{O_2},8}\, \dot{n}_8 - \dot{n}_{10} - x_{\mathrm{O_2},12}\, \dot{n}_{12} - x_{\mathrm{O_2},IV}\, \dot{N}_{IV}\right)$
11	$\frac{dP_{15}}{dt} = \frac{RT}{A_T\, L_{g,IX}} \left(\dot{n}_9 - \dot{n}_{15}\right) - \frac{P_{15}}{L_{g,IX}}\, \dot{L}_{g,IX}$
12	$\frac{dP_{16}}{dt} = \frac{RT}{A_T\, L_{g,X}} \left(\dot{n}_{10} - \dot{n}_{16}\right) - \frac{P_{16}}{L_{g,X}}\, \dot{L}_{g,X}$
13	$\frac{d\dot{n}_7}{dt} = \frac{1}{\tau_{equal}} \left(\dot{n}_{theo} - \dot{n}_7\right)$
14	$\frac{d\dot{n}_8}{dt} = \frac{1}{\tau_{equal}} \left(\dot{n}_{theo} - \dot{n}_8\right)$

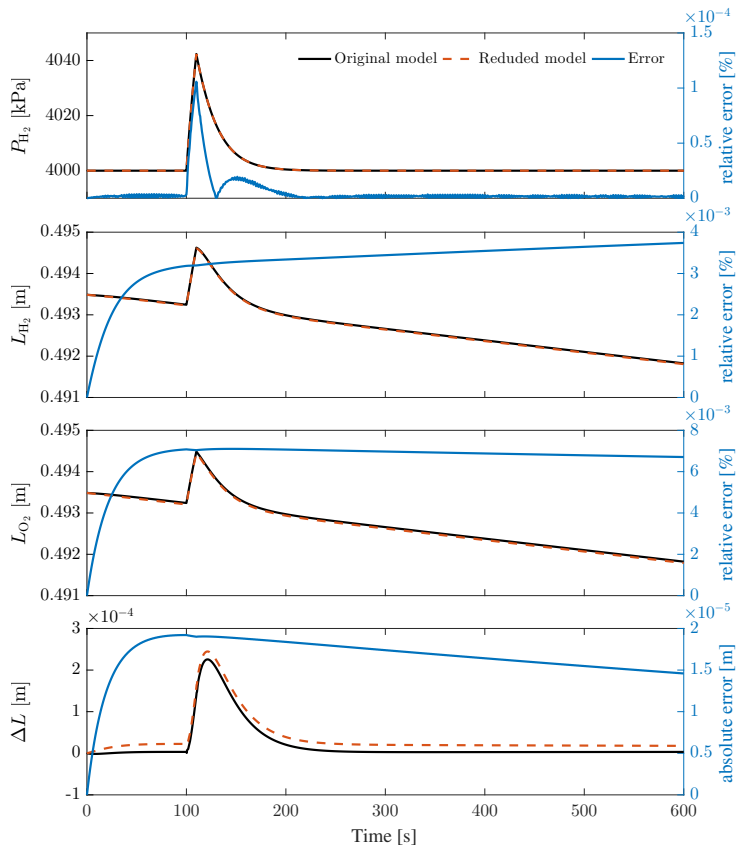

Figure 4: Comparison between the responses of the full nonlinear model and the reduced COM when a pulse of 10 s duration is applied in the current.

it can be observed that the pressure and levels in both separation chambers did not present differences while the difference in level has an increasing decoupling, although of small amount.

3. Control Design

In this section, two linear controllers are proposed for mitigating the cross-contamination of gases through the membrane in the alkaline electrolyzer presented in Section 2. The former is a classical PI control used frequently in industry, while the latter is a model-based $\mathcal{H}_\infty$ optimal controller.

In both cases, a linear model of the electrolyzer is required, therefore the operating conditions of the electrolyzer must be defined. Assuming the

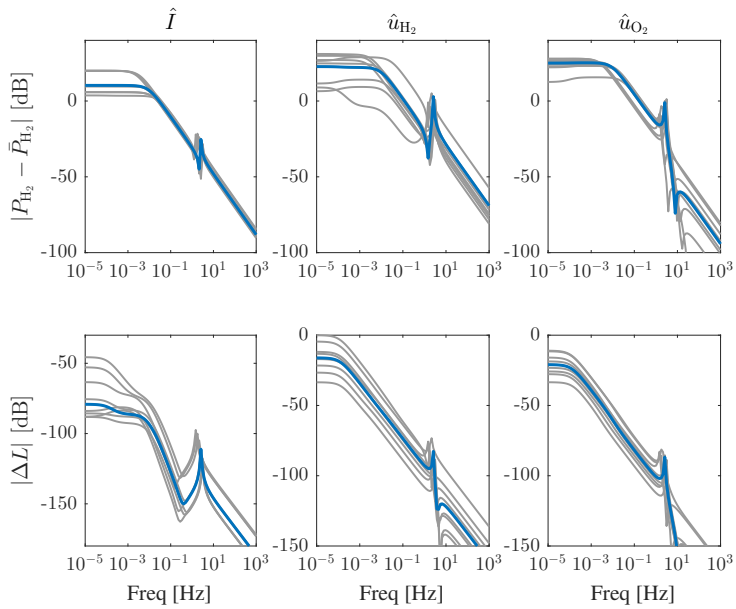

Figure 5: Frequency responses of the linearized model at several operating points (gray lines) and the nominal model $G(s)$ (blue lines).

control objective of tracking P_{ref} given in (8) and the regulation of ΔL around 0 are satisfied, the operating conditions can be parameterized by the steady-state values of the tank pressure $\bar{P}_{\text{tank}}$ and the current $\bar{I}$. Thus, the system operating region is defined as

$$\mathcal{O} = \left\{ (\bar{P}_{\text{tank}}, \bar{I}) \, : \, 0 \text{ kPa} \leq \bar{P}_{\text{tank}} \leq 7000 \text{ kPa} \right. \\ \left. \text{and } 10 \text{ A} \leq \bar{I} \leq 50 \text{ A} \right\}.$$

Next, the reduced nonlinear model introduced in Section 2.3 is numerically linearized at a representative operating point $(\bar{P}_{\text{tank}}, \bar{I}) \in \mathcal{O}$. To select this point, the linearization is performed over a grid of operating points in $\mathcal{O}$. The magnitude of the frequency responses for these operating points is shown in Figure 5 in gray lines and the selected nominal model is represented by a thicker blue line. This nominal model will be used to design the considered linear controllers. It can be observed that there is no drastic changes in the frequency responses at different operating points. This fact suggests that linear controllers can achieve a suitable performance.

The selected nominal dynamics are approximated by the model

$$y(s) = G(s)\begin{bmatrix}\hat{I}(s)\\ \hat{u}(s)\end{bmatrix} = \begin{bmatrix}G_d(s) & G_c(s)\end{bmatrix}\begin{bmatrix}\hat{I}(s)\\ \hat{u}(s)\end{bmatrix}, \tag{9}$$

where

$$\hat{u} = \begin{bmatrix}\hat{u}_{\mathrm{H_2}}\\ \hat{u}_{\mathrm{O_2}}\end{bmatrix} = \begin{bmatrix}u_{\mathrm{H_2}} - \bar{u}_{\mathrm{H_2}}\\ u_{\mathrm{O_2}} - \bar{u}_{\mathrm{O_2}}\end{bmatrix}, \qquad y = \begin{bmatrix}P_{\mathrm{H_2}} - \bar{P}_{\mathrm{H_2}}\\ \Delta L\end{bmatrix}.$$

The variable $\hat{u}$ is the vector of control inputs, and y is the vector of the controlled variables. The incremental current $\hat{I} = I - \bar{I}$ acts as a disturbance to be rejected. All of these variables are incremental values with respect to $\bar{I}$, $\bar{u}_{\mathrm{H_2}}$, $\bar{u}_{\mathrm{O_2}}$, and $\bar{P}_{\mathrm{H_2}}$, where the last three variables are functions of the operating point $(\bar{P}_{\mathrm{tank}}, \bar{I})$.

The first controller to be designed is based on classical PI design methods.

3.1. PI control

The system to be controlled, namely as $G_c(s)$, has two control inputs and two controlled outputs. It can be observed in Figure 5 that the control loops are coupled and a multivariable approach is required.

The simplest control approach consists in decoupling the loops and then designing two independent controllers [26]. For this purpose, the plant is right-multiplied by the inverse of its DC-gain, that is,

$$G_{\mathrm{dec}}(s) = G_c(s)G_c(0)^{-1}. \tag{10}$$

Figure 6 compares the frequency response of the original and the decoupled plants, respectively. It can be observed that the diagonal elements dominate the dynamics and the off-diagonal present a small response in the frequency range of interest, as compared to the original nominal model $G_c(s)$.

The transfer functions corresponding to the diagonal elements of the decoupled plant present a dominant dynamic behaviour similar to a first-order system, i.e., it can be approximated by

$$G_{\mathrm{dec}}(s) \approx \begin{bmatrix}\frac{k_1}{s-a_1} & 0\\ 0 & \frac{k_2}{s-a_2}\end{bmatrix}, \tag{11}$$

where $a_1 = -0.0576$ rad/s, $k_1 = 0.0576$, $a_2 = -7.817 \times 10^{-4}$ rad/s, and $k_2 = 7.817 \times 10^{-4}$. Consider the PI controller for each channel j,

$$K_{\mathrm{PI}}(s) = k_{p,j}\frac{s - b_j}{s}, \tag{12}$$

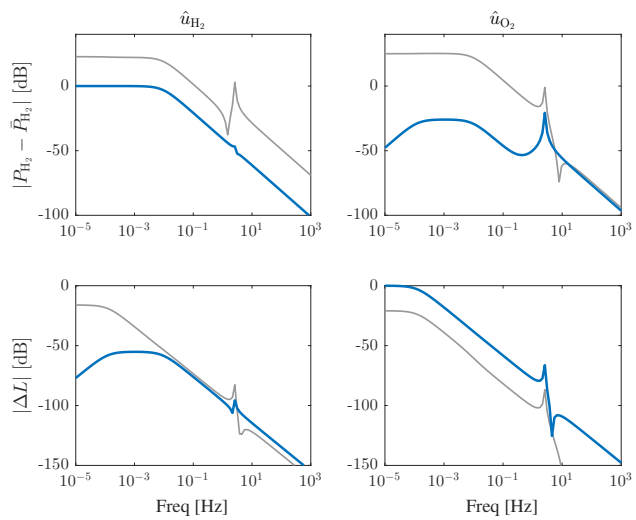

Figure 6: Frequency responses of the nominal plant $G_c(s)$ (gray lines) and decoupled plant $G_{\text{dec}}(s)$ (blue lines) used for the PI controller desing.

with $b_j = -k_{i,j}/k_{p,j}$ and being $k_{p,j}$ and $k_{i,j}$ the proportional and integral gains of the controller, respectively. Then, the controller parameters can be tuned by locating the zero b_j slightly at the left of the model dominant pole a_j and then adjusting the gain $k_{p,j}$ until a suitable closed-loop response is obtained.

The resulting closed-loop scheme combining the diagonal elements $G_{\text{dec},jj}(s)$, $(j = 1, 2)$ and the PI controllers is stable for all values of $k_{p,j}$. Nevertheless, a limit on these parameters comes from the lack of perfect decoupling, measurement noise levels, and the saturation of the control action. All these issues must be checked by simulation using the complete nonlinear model.

Next, a model-based robust controller will also be designed and compared with the previous one.

3.2. $\mathcal{H}_\infty$ optimal control

Alternatively, the controller can be designed in the frame of multivariable optimal control. In this case, the control design objectives are expressed as

$$\min_{\tilde{K}(s)} \frac{\|z\|_2}{\|w\|_2}, \tag{13}$$

where z is a performance variable and w a disturbance. Therefore, the controller design consists in defining a control setup and in selecting z and w according to the control specifications with suitable weighting functions [27, 28].

In the electrolyzer case, tracking a pressure reference P_{ref} while rejecting the disturbance I is sought. Hence, the performance variable z represents the pressure and level errors, and the disturbance w, of the system pressure and the current, i.e.,

$$z = W_e(s)M(s)\begin{bmatrix} P_{\text{H}_2} - P_{\text{ref}} \\ \Delta L \end{bmatrix}, \qquad w = W_u(s)\begin{bmatrix} P_{\text{ref}} \\ \hat{I} \end{bmatrix},$$

where

$$\begin{aligned} M(s) &= \begin{bmatrix} 1 & 0 \\ 0 & 1 \end{bmatrix}\frac{1}{s}, \\ W_e(s) &= \begin{bmatrix} k_{e,1} & 0 \\ 0 & k_{e,2} \end{bmatrix}, \\ W_u(s) &= \begin{bmatrix} k_{u,1} & 0 \\ 0 & k_{u,2} \end{bmatrix}\frac{s/0.1\omega_c + 1}{s/10\omega_c + 1}, \end{aligned}$$

being $k_{e,j}$, $k_{u,j}$ and ω_c design parameters. The weighting function $M(s)W_e(s)$ penalizes the low frequencies of the pressure and level errors and $W_u(s)$ penalizes the magnitude at high frequencies of the control actions. The closed-loop setup is shown in Figure 7.

The final controller is obtained after solving the optimization problem (13) and left-multiplying the resulting $\tilde{K}(s)$ by $M(s)$, that is,

$$K_\infty(s) = M(s)\tilde{K}(s). \tag{14}$$

This factorization is needed to ensure the existence of a stabilizing controller.

The order of the controller will be the order of the nominal model plus the order of all the weighting functions. Therefore, to simplify the real-time implementation, the order of $G(s)$ can be numerically reduced. As indicated in Section 3.1, the nominal model $G_c(s)$ exhibits a frequency response similar to a first-order system for each channel. Therefore, using a standard balanced-truncated reduction method [29], the linear time-invariant (LTI) nominal model of 14-th order is reduced by to a 2-nd order LTI model [27, 28]. The full and reduced models are compared in Figure 8. As observed in this figure, the reduced model is also dominated by two poles but is coupled unlike the model in Figure 6.

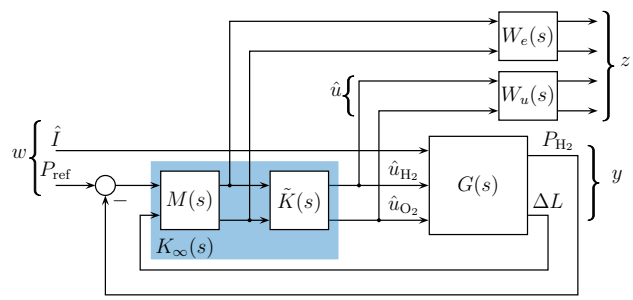

Figure 7: Control setup for the design of the $\mathcal{H}_\infty$ controller.

4. Simulation results

Numerical simulations were performed with the previously designed controllers combined with the full-nonlinear model of the electrolyzer. The simulations were performed in MatLab/Simulink with the variable-step solver Bogacki-Shampine (ode23), but other methods could also be used, e.g., Multistage Adomian decomposition method [30, 31, 32]. Two different scenarios were considered and discussed below. In the first situation, a large depressurization occurs while a constant electric current is applied. In the second scenario, the electrolyzer produces gases at constant pressure but the electric current fluctuates, as if it was provided by renewable energy sources. Previous reported results do not consider a dynamic model based on the phenomenology of the system for controller design, therefore a potential comparison with this work would be unfair.

The controllers were designed as indicated in Section 3. For the PI controller, the dominant poles of the decoupled plant are

$$a_1 = -0.0576\,\text{rad/s}, \qquad a_2 = -0.00078\,\text{rad/s}.$$

Therefore, the controller zeros were located at $b_j = 1.05\,a_j$ $(j = 1, 2)$ resulting in the following parameters:

$$k_{i,1} = 0.18, \qquad k_{p,1} = 3,$$
$$k_{i,2} = 0.16, \qquad k_{p,2} = 200.$$

For the $\mathcal{H}_\infty$ controller, the design parameters in the weighting functions were set as

$$k_{e,1} = 0.1, \qquad k_{e,2} = 4,$$
$$k_{u,1} = 0.8, \qquad k_{p,1} = 0.8,$$

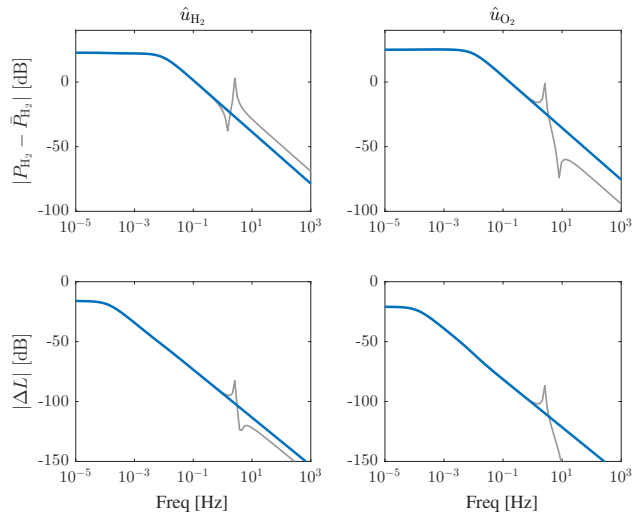

Figure 8: Frequency responses of the nominal plant $G_c(s)$ (gray lines) and of the reduced plant (blue lines) used in the $\mathcal{H}_\infty$ controller design.

and $\omega_c = 0.7$ rad/s.

4.1. Scenario 1: Depressurization

This scenario analyzes a depressurization process caused by a sudden change in the tank pressure P_{tank}. This pressure drop can be caused by a preparation for a prolonged maintenance shutdown or by the system management when low energy is forecasted.

Figure 9 shows the system responses with the PI controller (dashed lines) and the $\mathcal{H}_\infty$ controller (solid lines). In the upper plot, a sudden change of P_{tank} from 7000 to 1000 kPa and the reference P_{ref} computed according to (8) with a rate limit of 5 kPa/s, can be observed. The current density is required to remain constant at 0.21A/cm^2 (i.e., electric current $I = 30$ A). Both controllers achieve a suitable pressure reference tracking. There are more visible differences between both controllers in the evolution of level difference ΔL. The $\mathcal{H}_\infty$ controller achieves a faster convergence to the reference. On the other hand, impurity does not increase due to smooth control actions involving equalized pressures on both sides of the membrane. Instead, the impurity decreases due to the production of gases at a lower pressure. The goal of this simulation is to achieve a depressurization without extra contamination during this process, which is reached with both controllers. In Figure 9, it can be seen that the control actions u_{H_2} and u_{O_2} do not exceed the actuator limits.

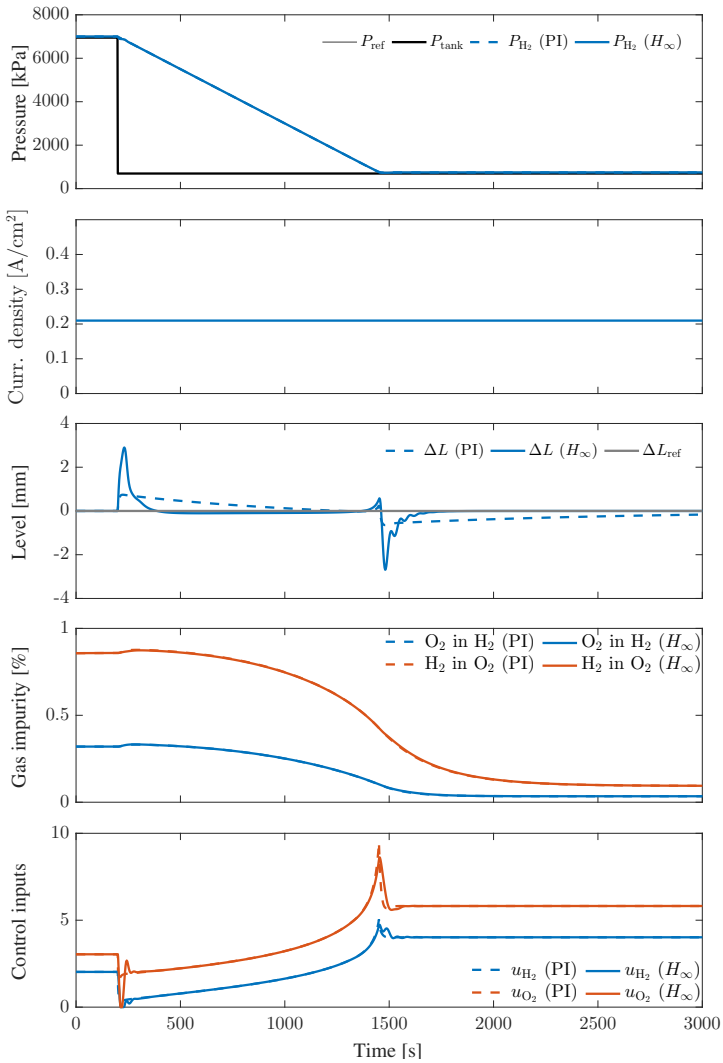

Figure 9: Simulation results corresponding to Scenario 1 using the PI controller (dashed lines) and the $\mathcal{H}_\infty$ controller (solid lines).

4.2. Scenario 2: Electric current fluctuations

In this scenario, the current density changes while the pressure reference P_{ref} is kept constant. The simulations using both controllers are compared in Figure 10. As can be seen, valves openings virtually follow the fluctuation of the current density due to the direct relationship between current density and gas production. Both controllers manage to maintain the reference pressure

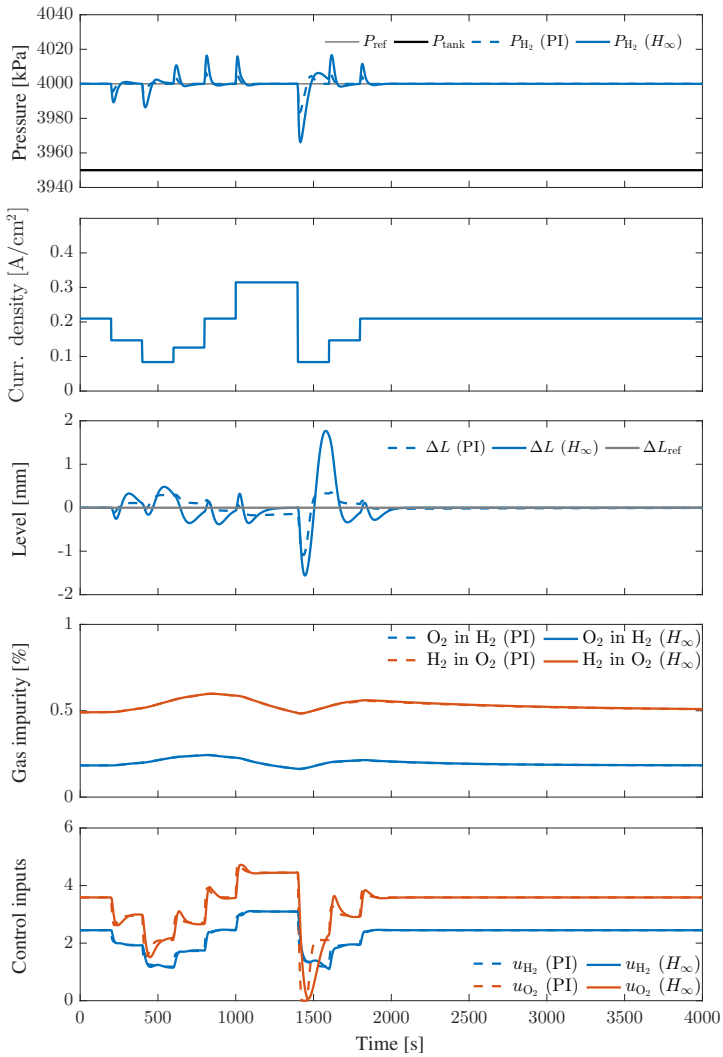

Figure 10: Simulation results corresponding to Scenario 2 using the PI controller (dashed lines) and the $\mathcal{H}_\infty$ controller (solid lines).

with a maximum error of 0.5% and the level difference in less than 2 mm. Because of this, O_2 impurity, that is always the highest value, is below 1%.

4.3. Controller comparison

Particularly in scenario 1, the $\mathcal{H}_\infty$ control has a higher transient error but converges to zero faster that in the PI case. Overall, the performance of both controllers is similar and depends on the tuning of the PI and the weight

selection for the $\mathcal{H}_\infty$ control procedure. Both controllers were designed from a common COM and seeking for the best performance/robustness compromise. In case of the PI controller, the tuning procedure consists in adjusting four parameters (the proportional and integral constants for each channel). In the $\mathcal{H}_\infty$ control, the design is based on an optimal algorithm and the controller is tuned by the proper selection of a set of weighting transfer functions. The PI controller might be preferred by some control engineers as it is based on a more intuitive SISO tuning procedure. However, this method relies on non-perfect decoupling that can affect the final closed-loop performance. Instead, the $\mathcal{H}_\infty$ controller requires more sophisticated design tools but is designed directly from the MIMO model in an optimal way, based on the performance/robustness weights that take care of low/high frequency requirements.

5. Conclusions

In the quest to raise the operating pressure of alkaline electrolyzers, control strategies are needed to decrease gas cross-contamination and, consequently, increase the purity of the supplied gases. In that sense, modelling and control are key issues in operation and design improvements. This work has proposed the design and comparison assessment of two different controllers that were tested in closed loop with a high-fidelity nonlinear model of the electrolyzer. They were able to maintain impurity below 1% in all cases, keeping the liquid solution level difference between both separation chambers below 4mm and a maximum pressure error of 0.5%.

Simulation results show that, with a suitable design, both controllers are capable of achieving satisfactory performance. Design and implementation issues will define which one is more practical. The design of the PI controller requires less model information, but a diagonalization stage needs to be made and the final parameters must be checked by extensive simulations. The $\mathcal{H}_\infty$ optimal controller algorithm is a multivariable system tool, the design is systematic and only depends on the selection of adequate robustness/performance weights.

6. Acknowledgement

This work has been partially funded by the Cheerful CSIC project (MHE-200065).

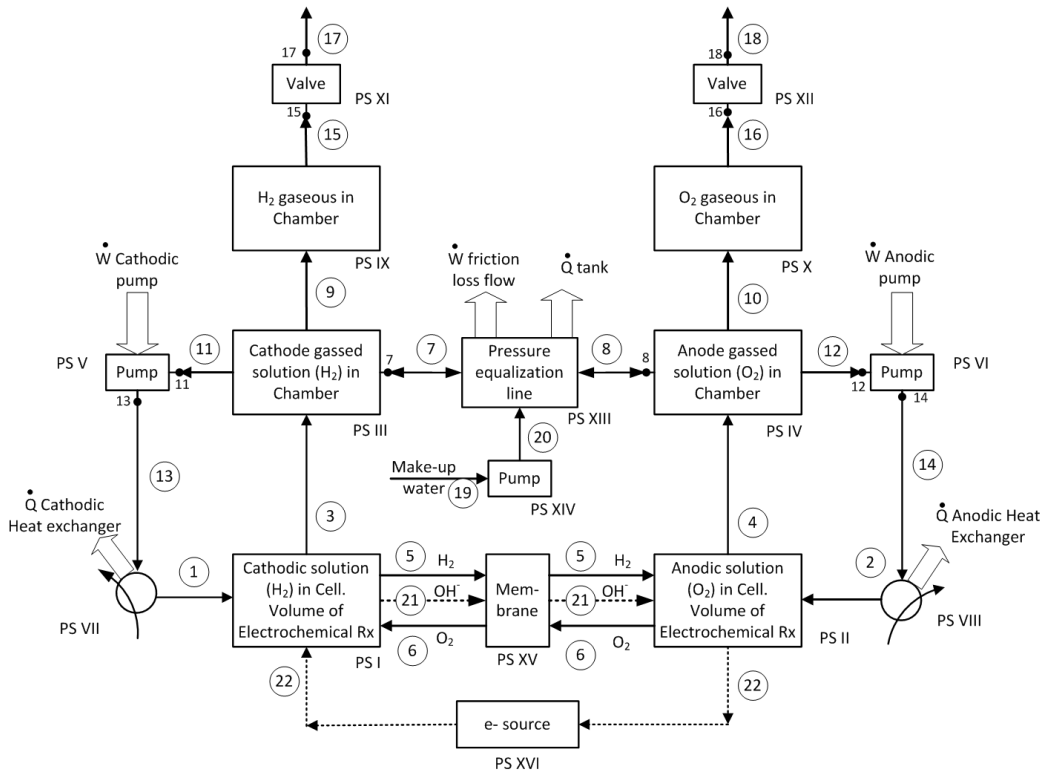

Figure A.11: Flow diagram with the PSs numbered in Roman. Mass flows are identified with numbers within circles. Taken from [19]

Appendix A. Summary of the complete nonlinear model

The PBSM is based on the flow diagram shown in Figure A.11, while a full description of the model is reported in [19]. A list of the ODEs governing the system behavior is given in Table A.2. This system has a clear symmetry between both lines: cathodic half-cell where H_2 is produced and anodic half-cell where O_2 is produced. Due to this symmetry, ODEs are similar between both lines. Therefore, in order to be concise, similar equations are presented once.

References

[1] I. E. Agency, Key world energy statistics 2019, IEA Paris (2019).

Table A.2: Balance equations forming the model basic structure. Adapted from [19]

State	Corresponding ODE
1	$\frac{d\bar{\rho}_3}{dt} = \frac{1}{V_{mix,I}} \left(\dot{n}_1 + \dot{n}_6 - \dot{n}_3 - \dot{n}_5 + r_1 \sum_i \sigma_{i,1}\right)$
2	$\frac{dx_{\mathrm{H_2},3}}{dt} = \frac{1}{N_I} \left(x_{\mathrm{H_2},1}\, \dot{n}_1 - x_{\mathrm{H_2},3}\, \dot{n}_3 - \dot{n}_5 + r_1 - x_{\mathrm{H_2},3}\, \dot{N}_I\right)$
3	$\frac{dx_{\mathrm{O_2},3}}{dt} = \frac{1}{N_I} \left(x_{\mathrm{O_2},1}\, \dot{n}_1 + \dot{n}_6 - x_{\mathrm{O_2},3}\, \dot{n}_3 - x_{\mathrm{O_2},3}\, \dot{N}_I\right)$
7	$\frac{dN_{III}}{dt} = \dot{n}_3 + \dot{n}_7 - \dot{n}_9 - \dot{n}_{11}$
8	$\frac{dL_{Lg,III}}{dt} = \frac{1}{A_{SC}} \left[\dot{V}_3 - \dot{V}_7 - \dot{V}_9 - \dot{V}_{11} + \dot{V}_{bubbles}\right)$
9	$\frac{dx_{\mathrm{H_2},III}}{dt} = \frac{1}{N_{III}} \left(x_{\mathrm{H_2},3}\, \dot{n}_3 + x_{\mathrm{H_2},7}\, \dot{n}_7 - \dot{n}_{\mathrm{H_2},9} - x_{\mathrm{H_2},11}\, \dot{n}_{11} - x_{\mathrm{H_2},III} \dot{N}_{III}\right)$
10	$\frac{dx_{\mathrm{O_2},III}}{dt} = \frac{1}{N_{III}} \left(x_{\mathrm{O_2},3}\, \dot{n}_3 + x_{\mathrm{O_2},7}\, \dot{n}_7 - \dot{n}_{\mathrm{O_2},9} - x_{\mathrm{O_2},11}\, \dot{n}_{11} - x_{\mathrm{O_2},III} \dot{N}_{III}\right)$
15	$\frac{dP_{15}}{dt} = \frac{RT}{A_T\, L_{g,IX}} \left(\dot{n}_9 - \dot{n}_{15}\right) - \frac{P_{15}}{L_{g,IX}}\, \dot{L}_{g,IX}$
16	$\frac{dx_{\mathrm{H_2},15}}{dt} = \frac{1}{N_{IX}} \left(x_{\mathrm{H_2},9}\, \dot{n}_9 - x_{\mathrm{H_2},15}\, \dot{n}_{15} - x_{\mathrm{H_2},15} \dot{N}_{IX}\right)$
17	$\frac{dx_{\mathrm{O_2},15}}{dt} = \frac{1}{N_{IX}} \left(x_{\mathrm{O_2},9}\, \dot{n}_9 - x_{\mathrm{O_2},15}\, \dot{n}_{15} - x_{\mathrm{O_2},15} \dot{N}_{IX}\right)$
21	$\frac{d\dot{n}_7}{dt} = \frac{1}{\tau_{equal}} \left(\dot{n}_{theo} - \dot{n}_7\right)$
23	$\frac{dN_{XIII}}{dt} = \dot{n}_{XIII,in} - \dot{n}_{XIII,out} + \dot{n}_{20}$
24	$\frac{dx_{\mathrm{H_2},XIII}}{dt} = \frac{1}{N_{XIII}} \left(x_{\mathrm{H_2},XIII,in}\, \dot{n}_{XIII,in} - x_{\mathrm{H_2},XIII,out}\, \dot{n}_{XIII,out} + A_{line} \Phi_{\mathrm{H_2}} - x_{\mathrm{H_2},XIII} \dot{N}_{XIII}\right)$

[2] B. Lux, B. Pfluger, A supply curve of electricity-based hydrogen in a decarbonized european energy system in 2050, Applied Energy 269 (2020) 115011–115030.

[3] J. Gorre, F. Ortloff, C. van Leeuwen, Production costs for synthetic

methane in 2030 and 2050 of an optimized power-to-gas plant with intermediate hydrogen storage, Applied Energy 253 (2019) 114594–114604.

[4] M. David, C. Ocampo-Martinez, R. Sánchez-Peña, Advances in alkaline water electrolyzers: A review, Journal of Energy Storage 23 (2019) 392–403.

[5] S. Wang, B. Tarroja, L. Smith Schell, B. Shaffe, S. Scott, Prioritizing among the end uses of excess renewable energy for cost-effective greenhouse gas emission reductions, Applied Energy 235 (2019) 284–298.

[6] K. Kavadias, D. Apostolou, J. Kaldellis, Modelling and optimisation of a hydrogen-based energy storage system in an autonomous electrical network, Applied Energy 227 (2018) 574–586.

[7] T. Mahlia, T. Saktisahdan, A. Jannifar, M. Hasan, H. Matseelar, A review of available methods and development on energy storage: technology update, Renewable and Sustainable Energy Reviews 33 (2014) 532–545.

[8] F. Dawood, M. Anda, G. Shafiullah, Hydrogen production for energy: An overview, International Journal of Hydrogen Energy 45 (2020) 3847–3869.

[9] J. O. Abe, A. P. I. Popoola, E. Ajenifuja, O. M. Popoola, Hydrogen energy, economy and storage: review and recommendation, International Journal of Hydrogen Energy 44 (2019) 15072–15086.

[10] M. Schalenbach, A. R. Zeradjanin, O. Kasian, S. Cherevko, K. J. Mayrhofer, A perspective on low-temperature water electrolysis – challenges in alkaline and acidic technology, International Journal of Electrochemical Science 13 (2018) 1173–1226.

[11] P. Haug, B. Kreitz, M. Koj, T. Turek, Process modelling of an alkaline water electrolyzer, International Journal of Hydrogen Energy 42 (2017) 15689–15707.

[12] J. Milewski, G. Guandalini, S. Campanari, Modeling an alkaline electrolysis cell through reduced-order and loss-estimate approaches, Journal of Power Sources 269 (2014) 203–211.

[13] M. Hammoudi, C. Henao, K. Agbossou, Y. Dubé, M. Doumbia, New multi-physics approach for modelling and design of alkaline electrolyzers, International Journal of Hydrogen Energy 37 (2012) 13895–13913.

[14] E. Amores, J. Rodríguez, C. Carreras, Influence of operation parameters in the modeling of alkaline water electrolyzers for hydrogen production, International Journal of Hydrogen Energy 39 (2014) 13063–13078.

[15] O. Ulleberg, Modeling of advanced alkaline electrolyzers: a system simulation approach, International Journal of Hydrogen Energy 28 (2003) 21–33.

[16] W. Hug, J. Divisek, J. Mergel, W. Seeger, H. Steeb, Intermittent operation and operation modelling of an alkaline electrolyzer, International Journal of Hydrogen Energy 18 (12) (1993) 973–977.

[17] M. Sánchez, E. Amores, D. Abad, L. Rodríguez, C. Clemente-Jul, Aspen plus model of an alkaline electrolysis system for hydrogen production, International Journal of Hydrogen Energy 45 (2020) 3916–3929.

[18] M. David, H. Alvarez, C. Ocampo-Martinez, R. Sánchez-Peña, Phenomenological based model of hydrogen production using an alkaline self-pressurized electrolyzer, in: 18th European Control Conference (ECC), 2019, pp. 4344–4349.

[19] M. David, H. Alvarez, C. Ocampo-Martinez, R. Sánchez-Peña, Dynamic modelling of alkaline self-pressurized electrolyzers: a phenomenological-based semiphysical approach, International Journal of Hydrogen Energy 45 (43) (2020) 22394–22407.

[20] P. Olivier, C. Bourasseau, P. B. Bouamama, Low-temperature electrolysis system modelling: A review, Renewable and Sustainable Energy Reviews 78 (2017) 280–300.

[21] F. Vivas, F. De las Heras, A.and Segura, J. Andújar, A review of energy management strategies for renewable hybrid energy systems with hydrogen backup, Renewable and Sustainable Energy Reviews 82 (2018) 126–155.

[22] G. Gahleitner, Hydrogen from renewable electricity: An international review of power-to-gas pilot plants for stationary applications, International Journal of Hydrogen Energy 38 (2013) 2039–2061.

[23] C. A. Schug, Operational characteristics of high-pressure, high-efficiency water-hydrogen-electrolysis, International Journal of Electrochemical Science 23 (1998) 1113–1120.

[24] M. Schalenbach, G. Tjarks, M. Carmo, W. Lueke, M. Mueller, D. Stolten, Acidic or alkaline? towards a new perspective on the efficiency of water electrolysis, Journal of the Electrochemical Society 11 (2016) 3197–3208.

[25] F.-W. Speckmann, S. Bintz, K. P. Birke, Influence of rectifiers on the energy demand and gas quality of alkaline electrolysis systems in dynamic operation, Applied Energy 250 (2019) 855–863.

[26] K. J. Aström, T. Hägglund, Advanced PID control, Instrumentation, Systems, and Automation Society, Research Triangle Park, USA, 2006.

[27] K. Zhou, J. C. Doyle, K. Glover, Robust and Optimal Control, Prentice Hall, 1996.

[28] R. Sánchez-Peña, M. Sznaier, Robust System Theory and Applications, Wiley & Sons, 1998.

[29] K. Glover, All optimal Hankel-norm approximations of linear multivariable systems and their L_∞ error bounds, International Journal of Control 39 (6) (1984) 1115–1193.

[30] H. Fatoorehchi, M. Alidadi, R. Rach, A. Shojaeian, Theoretical and experimental investigation of thermal dynamics of steinhart–hart negative temperature coefficient thermistors, Journal of Heat Transfer 141 (7) (2019) 072003.

[31] H. Fatoorehchi, H. Abolghasemi, R. Zarghami, Analytical approximate solutions for a general nonlinear resistor–nonlinear capacitor circuit model, Applied Mathematical Modelling 39 (19) (2015) 6021–6031.

[32] J.-S. Duan, R. Rach, A.-M. Wazwaz, A reliable algorithm for positive solutions of nonlinear boundary value problems by the multistage adomian decomposition method, Open Engineering 5 (1) (2014) 59–74.